Composite Structures 147 (2016) 197–210

Contents lists available at ScienceDirect

Composite Structures

journal homepage: www.elsevier.com/locate/compstruct

Laser Doppler imaging of delamination in a composite T-joint with remotely located ultrasonic actuators

G. Kolappan Geetha [a], D. Roy Mahapatra [a,*], S. Gopalakrishnan [a], S. Hanagud [b]

[a] Department of Aerospace Engineering, Indian Institute of Science, Bangalore 560012, India
[b] School of Aerospace Engineering, Georgia Institute of Technology, Atlanta, GA 30332-0150, USA

ARTICLE INFO

Article history:
Received 16 November 2015
Revised 4 March 2016
Accepted 24 March 2016
Available online 25 March 2016

Keywords:
Lamb wave
Ultrasonic
LDV
Delamination
T-joint
Mode conversion

ABSTRACT

This paper presents an experimental study on the interaction of ultrasonic guided waves with delamination in the web–flange interface of a co-cured, co-bonded composite T-joint. A complex interaction of waves is induced, first, by one, and, later, by two piezoceramic wafer(s) bonded on the inner surface of the flange. The flange surface velocity distributions are reconstructed from the scanning laser Doppler velocimeter (LDV) measurements to study the effect of a delamination overlapping the web–flange interface. The surface-bonded piezoelectric actuator(s) placed remotely on the flange produce primarily anti-symmetric wave incidence to the delamination. A two-stage wave mode conversion process, one due to the web and joint filler, and the other due to the delamination underneath the flange is observed. First, we address the problem of identification of delamination by ultrasonic contrast imaging of the web–flange interface using a single actuator. This study is extended further to enhance the ultrasonic contrast imaging at the web–flange interface using a standing wave. A quantitative methodology based on mode conversion strength is developed to monitor different structural features like free-edge, web–flange interface and delamination. The results show the complex nature of the conversion of flexural waves to in-plane waves through the deltoid and along the web–flange interface.

1. Introduction

Integrally designed and fabricated composite structural joints have several advantages such as a high strength to weight ratio, very good endurance against fatigue and wear, good corrosion resistance etc. Despite these advantages, quality control in the manufacturing of composite joined structures is highly demanding and subsequently the structure requires reliable inspection at periodic intervals to detect possible defects. An assembly of complex composite structures often requires efficient joining in the form of T-joints or T-stiffeners. The usage of co-cured, co-bonded composite T-joints in aerospace vehicles can result in a total reduction of structural components (bolts/fasteners) by 30% compared to the metallic structure [1]. The main part of the T-joint includes a flange, web, and radius filler. In a typical composite stiffened airframe, the flange interfaces with the skin; the web provides an interface for attachment of the substructure, and the radius filler provides continuity of load transfer between the web and flange. The T-joint transfers flexural, tensile, and shear loads from the skin to the web besides acting as a stiffener to carry bending and buckling loads directly. Particular design objectives involve, for example, the prevention of skin buckling during wing loading, increase of bending/torsional strength of the integral payload, a fuel tank attached to the airframe, etc.

A survey of the aircraft industry highlights the cost of maintenance per annum for ageing aircraft structures to the tune of about one-third of the aircraft cost [2]. According to another survey [3], about 90% of the aircraft structures skin inspections are conducted using visual inspections [4] and remaining the 10% are conducted using various other Non-Destructive Inspection techniques such as dye penetration [5], eddy current [6], radiography [7], ultrasonics [8] etc. Reviews of the current state-of-the-art of various Non-Destructive Inspection (NDI) techniques for composite structures with their limitations can be found in Ref. [9] and further references therein. Life extension of the ageing aircraft using embedded Fiber Bragg Grating (FBG) based Structural Health Monitoring on composite structures are described in Ref. [10]. The deployment of the NDI techniques mentioned above are restricted by the nature of disassembly required for complex structural components, geometry/material specific probes and associated attachments, and the level of accessibility to the damage(s).

* Corresponding author.
E-mail address: droymahapatra@aero.iisc.ernet.in (D. Roy Mahapatra).

http://dx.doi.org/10.1016/j.compstruct.2016.03.039
0263-8223/

Structural Health Monitoring (SHM) is the continuous, autonomous in-service monitoring of the physical condition of a structure by means of embedded/contact/non-contact sensors with minimal manual intervention [11]. It is aimed at assuring the structural integrity of the aircraft, replacing periodic scheduled based maintenance to condition based maintenance. The key motivations for SHM include gain over maintenance and design benefits. Maintenance aspects are increasingly significant for the reduction of Direct Operating Costs (DOC), since fuel bills, airport fees, etc. have little potential in saving expenses. Reduction of Direct Maintenance Cost (DMC) increases the availability of aircrafts. The motivation to use SHM for innovative design approaches is the need of the manufactures to offer aircraft with increased fuel efficiency. SHM will be used to get new concepts for structural design, which will lead to weight reduction for metal and composite structures up to 15% on component level [12]. The final idea of SHM is to imitate human nervous system.

In the present paper, we explore a new methodology and experimental results, which may be useful in addressing some of the problems above, particularly for monitoring inaccessible features and damage(s) in composite structures. Vibration/modal analysis-based methods for the detection of small damage(s) are less sensitive when compared to ultrasonic wave propagation based methods [13]. Wave propagation-based diagnose using ultrasonic guided waves have been demonstrated quite effectively in metallic structures with cracks [14], fatigue damage [15], corrosion [16] etc. and also for composites for debonding [17], delamination [18–20], matrix cracking [21] etc. Ultrasonic wave propagation in inhomogeneous and anisotropic media and the application of the wave characteristic based finite element method for efficient damage detection for Structural Health Monitoring (SHM) have been developed (see Ref. [22] and references therein). A mechanistic treatment explaining how guided waves are influenced due to delaminations and cracks in composite beams is discussed in Refs. [19,23,24]. This explanation helps in developing specialized schemes of damage detection.

Piezoelectric Wafer Active Sensors (PWAS) bonded on composite structures can be designed to perform integrated SHM using Lamb waves [25]. Optimization studies involving actuator and sensor configuration(s), types of excitation signals and procedures for the diagnosis of pre-existing damage(s) such as delamination, matrix crack(s), through thickness hole(s) etc. in test coupons have been reported in Ref. [26]. The distributed sensing behavior of piezoceramic patches embedded in composites subjected to static and dynamic fracture has been studied in Ref. [27,28]. The delamination of composite panels and joints due to impact loads is a major concern. Low velocity impact damage has been identified using the amplitude of the piezoelectric sensor signal [29]. Damage in composites has been identified using distributed piezoelectric transducers [30]. Ultrasonic signal focusing and steering in isotropic plates by an array of transmitters using a delay-and-sum algorithm have been reported in Ref. [31,32]. Due to the directional dependencies of group velocities in anisotropic composites, the slowness curve is not circular [33]. Furthermore, for dispersive guided waves, there is a different slowness curve for each frequency of every wave mode. Yan et al. [34] have demonstrated that, for certain frequencies, the slowness curve for a specific mode can be nearly circular, and under such a condition the delay-and-sum algorithm can be applied to ultrasonically scan a probable damage area. The effect of delamination in Carbon Fiber Reinforced Polymer (CFRP) plates on the lobe pattern has been analyzed using a linear phased array of piezoelectric transducers [35]. Ultrasonic wave field imaging with non-contact LDV is another offline NDI technique that can efficiently utilize actuator-induced ultrasonic guided waves and the surface velocity scan data can be algorithmically analyzed, thereby minimizing physical hardware complexity for focusing and steering ultrasound through probable damage zones. The problem of detecting delamination in composites and identifying the size, particularly when the delamination is in the joint, is addressed in the present paper. This is a challenging problem as nearby structural boundaries alter the propagation of a guided wave. A brief summary of a damage diagnosis and structural wave field imaging using LDV is given below before we illustrate our scheme of delamination imaging in a composite T-joint.

While performing an ultrasonic C-scan of the joints, the ultrasonic wave is deflected in different directions, and, hence, the received amplitude is less, leading to a dark area in the C-scan image. By using non-contact ultrasonic sensors, the problems due to liquid couplants or dry couplants and the associated variations in signal sensitivity due to an impedance mismatch between the couplant and the structure etc. can be avoided. Among the various different laser-based techniques for vibration measurement, such as holography, Electronic Speckle Pattern Interferometry (ESPI), shearography, and laser Doppler velocimeter (LDV), we consider LDV in our present research. One of the distinct advantages of LDV is its high sensitivity to the high frequency vibration of optically reflecting surfaces. LDV-based studies involving small/large area sensing and damage diagnose can be found in Refs. [36–43]. Vibration excitation at a single point using a physically wired transducer and measuring the structural dynamic response at various points using LDV is commonly employed. Ultrasonic imaging using non-contact laser excitation at multiple points and a structural dynamic response at a single point without scanning has been demonstrated in metallic and composite structures by Sohn et al. [41–43]. This method is based on the principle of the linear reciprocity of ultrasonic waves. This reciprocity relation does not hold when the wave path is not reversible. This irreversibility of the wave path may be a factor if multiple dissimilar transducers are used for actuation/sensing, or when the time windows of sensing at various different points are different or when boundary scattering appears in a certain propagation path that disturbs the reciprocity of the wave field. Another practical limitation here is the measurements involving boundary scattering due to which the uniqueness of the wave path is lost. Alternatively, an ultrasonic contrast-based imaging method is developed in the present study. Subsequently, we propose the concept of a standing wave filter and a Laplacian image filter that clearly improve the image contrast. These are highly effective in regions where the waves experience multiple reflections and transmissions from the defect boundary. The technique poses certain limitations in cases where the defect boundary overlaps with the structural features as in the case of a delamination overlapping with the web–flange interface. In this case, the defect boundary may not be clearly distinguished from the structural feature boundary.

Frequency–wavenumber filtering is another approach where boundary reflection may be separable if an accurate model of boundary reflection is known [44]. The formulation of damage indices based on strain energy and techniques like spatial decimation and frequency–wavenumber filtering have been reported in Ref. [45]. However, the ultrasonic contrasting of an inaccessible zone in the rear-field for a complex-shaped structure poses significant challenges. The applications of wave filters are also limited as they assume unidirectional propagation of a single wave mode at a time, whereas structures like composite T-joints produce near-field conversion of various wave components in various different directions. The present effort is the first of its kind to resolve the complexities involved and to quantify wave mode conversion near the vicinity of a delamination.

The paper is organized as follows: first, the fabrication process for a composite T-joint test specimen is described in Section 2. The details of the actuation and sensing schemes are explained in Section 3. The mathematical modeling background for the

analysis of wave propagation and wave field images captured using 3D LDV are given in Section 4. Complex ultrasonic wave field interactions due to the web and joint filler on the back face of the flange, and those due to a delamination underneath the flange are analyzed in Section 5. The method of ultrasonic contrast enhancement surrounding the web–flange interface and the delamination, using the concept of standing waves in real time, is discussed next. Standing waves eliminate the need for frequency–wavenumber filtering of unwanted scattering of boundary features (web–flange interface). The identification and classification of structural features using ultrasonic guided wave mode conversion strength and various possibilities are discussed in Section 5.

2. Test specimen of composite T-joint with delamination

In order to manufacture a composite T-joint, a mould is made using high-carbon SAE 304 stainless steel. The different parts of the disassembled mould are shown in Fig. 1(a). Proper clearances in the mould accommodate resin over-flow during the manufacturing of the T-joint by the Resin Transfer Moulding (RTM) method. The inner surfaces of the mould are coated with one-sided adhesive film to prevent direct contact of the mould with epoxy and for easy release of the specimen with a good surface finish. Uni-directional glass fabrics having 0°, 45°, and 90° fiber orientations and required dimensions are cut (Fig. 1(c)). Resin (30 wt%) is applied and the fabric layers are stacked by the wet lay-up method. E-glass fibers with Araldite 5052 resin system are used for manufacturing co-cured co-bonded composite T-joint. Different parts of the mould are then assembled (Fig. 1(d)) and the entire mould is enclosed within a vacuum bag (Fig. 1(g)). The test specimen is cured at room temperature in a vacuum bag for 24 h. In order to ensure proper compaction, a static load is applied over the top of the assembled mould in addition to the differential pressure due to the vacuum bag (see Fig. 1(e) and (f)). A Teflon tape of dimension 50 mm × 30 mm × 0.25 mm is introduced at the desired location to simulate a delamination underneath the accessible side of the flange. The delamination is introduced between third and fourth layers, underneath the accessible side of the flange. It is at a depth of approximately 0.75 mm from the accessible side of the flange. The delamination created in this manner is marked in Fig. 3(c). The dimensions of the flange and the web of the final test specimen (see Fig. 3(a)) are 260 mm × 125 mm × 2 mm and 260 mm × 75 mm × 2 mm, respectively. The test specimen has a quasi-isotropic ply stacking sequence $(0/90/+45/-45)_s$ both in the flange as well as in the web.

3. Experimental Setup

A 3D LDV (model PSV 3D 400 Polytec) having three independent laser beams for Doppler measurement is used in the present

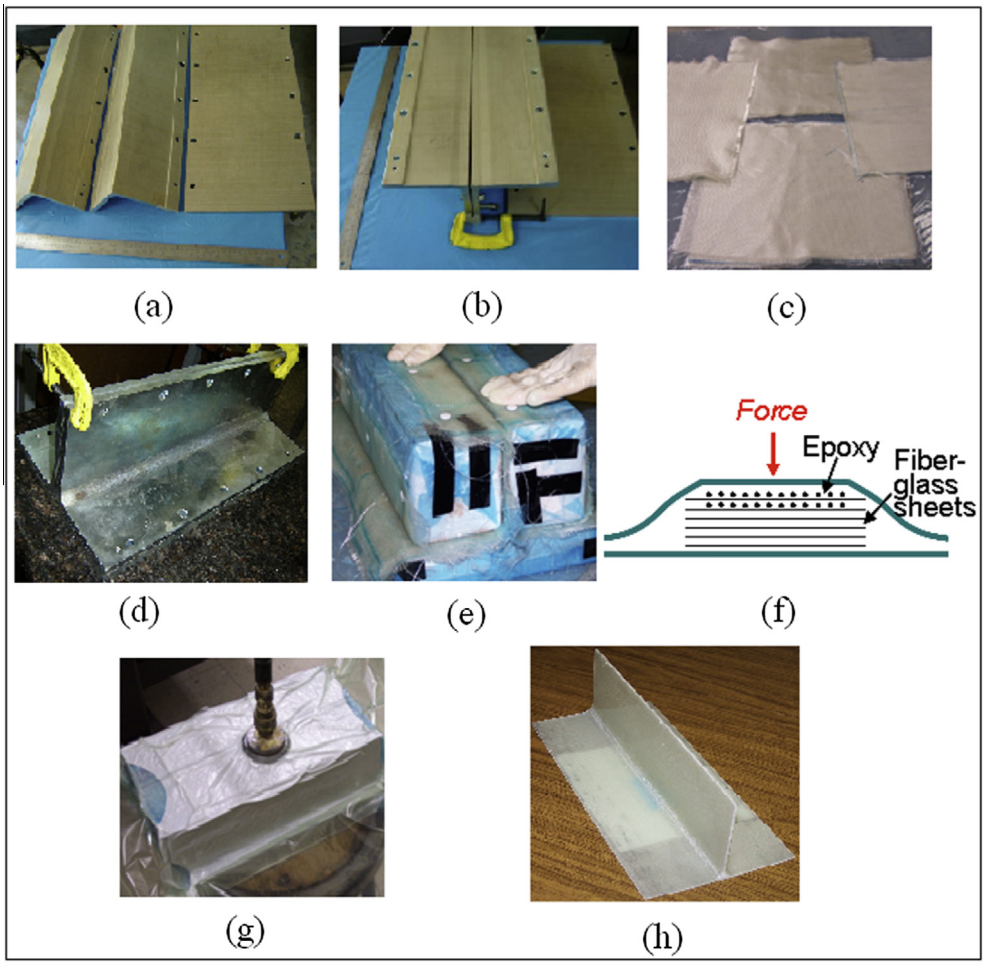

Fig. 1. (a) Disassembled view of different parts of composite T-joint mould. (b) Assembled view of the mould which is coated with one-sided adhesive film to prevent direct contact with epoxy. (c) Uni-directional glass fibre fabric of required dimension cut from glass fabric roll. (d) Assembled view of mould during manufacturing of composite T-joint. (e) A static load is applied over the top of the assembled mould to ensure proper compaction. (f) Schematic diagram showing application of static load to ensure proper compaction. (g) The entire mould is enclosed within a vacuum bag for curing under high compaction pressure at room temperature. (h) The final T-joint test specimen having delamination overlapping the web–flange interface.

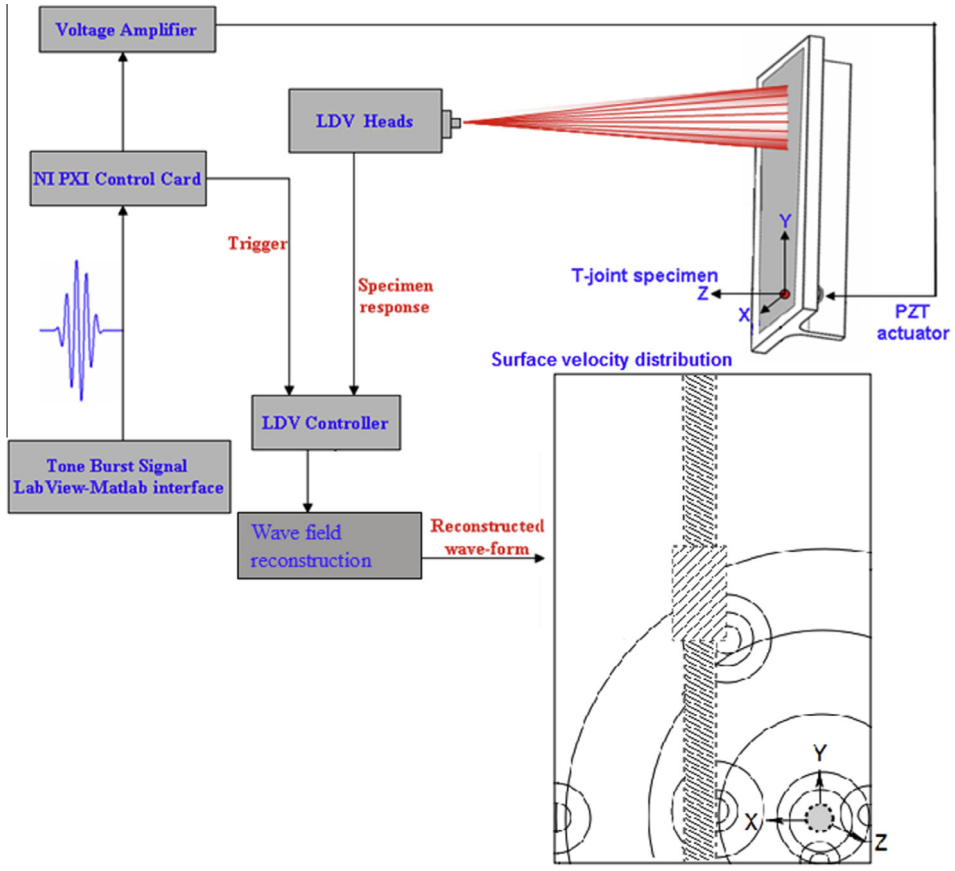

Fig. 2. The schematic operation of LDV measurement system synchronized with Controller and Data Acquisition System (DAQ).

experiment. Its measurement principle is based on the Doppler shift produced by an incident laser light and backscattered light by the vibrating surface of the test structure when excited by ultrasound. According to the Doppler shift, the change in the wavelength of the backscattered light is a function of the relative velocity of the vibrating surface. The velocity of the vibrating surface is obtained by measuring the change in the wavelength of the backscattered laser light, which forms an interference fringe pattern. Thus, LDV works as a non-contact ultrasonic sensor with a long standoff distance. A motorized mirror on each of the three-laser beam paths enable velocity time history to be measured seamlessly over software-controlled grid-points on the structural surface. Distinct measurements at two very nearby points is possible as the spot size of the laser beam is less than 10 μm, whereas a typical bonded PWAS would occupy a much larger area. The velocity components along the three beam directions are transformed to structural coordinates knowing the relative orientation of the beams with respect to a workplane with the help of encoders. LDV, being a non-contact measurement system, eliminates sensor near-field signal distortion and damping as usually encountered in bonded PWAS.

The maximum grid spacing for the measurement of velocity distribution on the surface of interest is taken as one-tenth of wavelength (λ). λ is computed based on the frequency of excitation and the group velocity dispersion curve for the composite specimen on which the scan is being done. This is obtained based on a suitable model of wave propagation or experimentally. The Z component usually refers to the surface normal direction while the X–Y plane defines the surface. The accuracy of the signals is primarily limited by the laser speckle noise.

The ultrasonic wave excitation hardware consists of an NI PXI-6115 multi-channel A/D and D/A card, a voltage amplifier and piezoelectric PZT actuator(s). A tone-burst voltage signal with prescribed frequency content and amplitude is fed to the actuator. The piezo actuator is of 15 mm diameter and 1.5 mm thickness and bonded to the composite using an epoxy resin based adhesive. The wave modes induced by the actuator consist of a dominant fundamental antisymmetric (A0) component and a negligible fundamental symmetric (S0) component during the initial stage of propagation. However, S0 components with significantly large amplitudes are induced due to A0 → S0 conversion in the composite due to the ply stacking and the material interfaces and delamination. A schematic view of the experimental setup is shown in Fig. 2.

4. Experimental procedure

Fig. 3 shows the composite T-joint with a coordinate reference frame, position of the actuator, and a delamination and flange surface with grid points for LDV measurement. The T-joint with the actuator is placed on a mechanical fixture and the flange surface, as marked in Fig. 3(b), is exposed to a laser beam. The surface being scanned is the accessible surface (exterior of the integral skin) in the desired application of interest. In the present experiment, the grid for the scan consists approximately of 30,000 scan points with 0.9 mm spacing along both the X and Y directions for an A0 wavelength of 11 mm and a signal carrier frequency of 100 kHz. A band-pass filter with a narrow frequency band of 5 kHz is used. The signal sampling frequency is set, 10 times greater than the excitation frequency (signal carrier frequency). The details of various

parameters like the number of samples, pre-trigger, and the type of velocity decoder used in A/D settings are given in Table 1.

4.1. Ultrasonic signal characteristics

The signal frequency for interrogation is chosen considering various factors. Most important among them are (i) the dispersion characteristics of the scan region, and (ii) the Signal-to-Noise Ratio (SNR). The type and shape of the diagnostic waveform selected is decided based on the dispersive nature of the medium and the separability of the scattered packets depending on the size of the structure. A five-cycle windowed sine signal (tone-burst signal) is used for damage diagnostics (see Fig. 4) in the present study. A Hanning window is used to concentrate a maximum of energy around the desired carrier frequency. The narrower the bandwidth of excitation, the lower is the dispersive effect distorting the wave packet as it propagates in the composite. The tone-burst excitation signal is generated periodically with repeating time windows to enable multiple measurements at each grid point and the sequence is repeated over the entire grid. A suitable time delay is introduced between each time window in this sequence. This avoids overlapping measurements at each scan point, and provides sufficient time for the reverberant waves to damp out.

Table 1
LDV measurement details.

Testing parameters	Parameter values
Excitation frequency	100 kHz
Filter	Bandpass filter (97.5–102.5 kHz)
Sampling frequency	2.56 MHz
Number of samples	1024
Sample time	400 μs
Pre-trigger	10% Sample time
Total scan points	30,761
Range of decoder	VD-07 50 mm/s/V
Excitation voltage	40 V
Time delay between each trigger (dt)	5 s

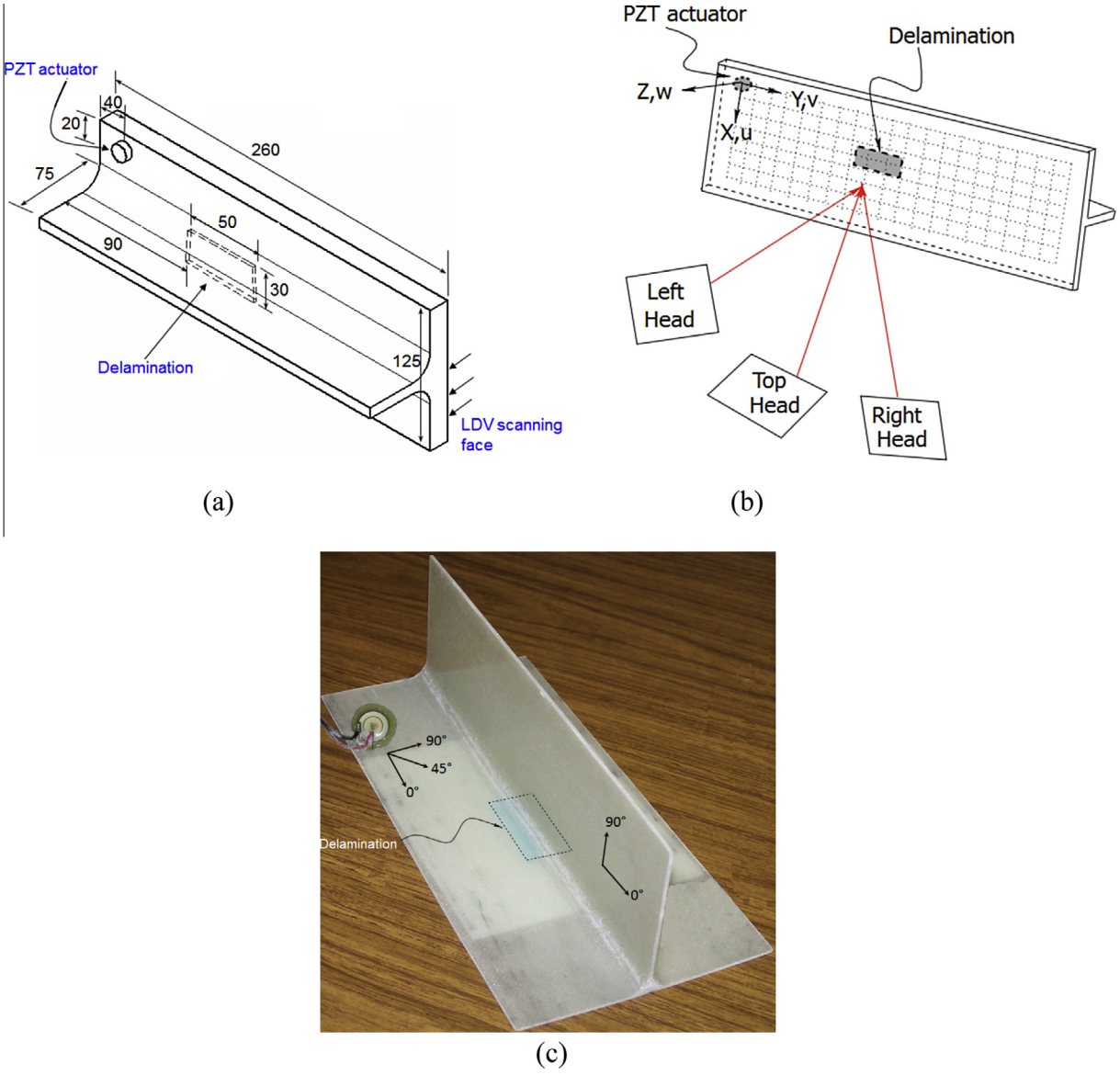

Fig. 3. (a) Schematic showing dimensions of T-joint specimen with piezo wafer actuator and delamination in the web–flange interface. (b) The Cartesian coordinate system of T-joint test specimen with respect to LDV laser heads. (c) Detailed view of T-joint test specimen with fiber orientation, delamination and piezo actuator. All units are in mm.

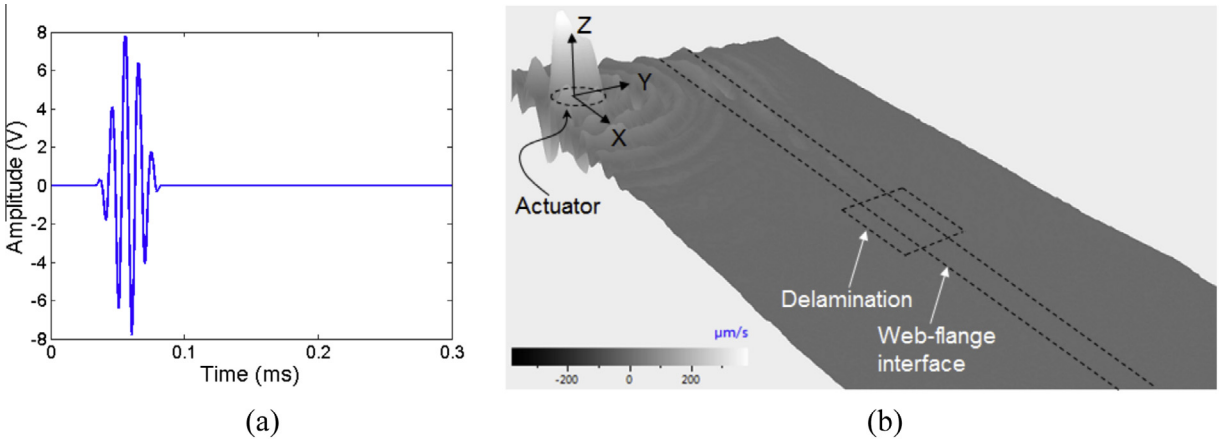

Fig. 4. (a) Five cycle tone-burst signal applied to piezo actuator. (b) Wave field visualization near the zone of piezo actuator at 56 μsec.

4.2. Evaluating wave dispersion characteristics

Besides the direct estimation of group velocity dispersion through experiments, it is often necessary to evaluate the dispersion characteristics and identify wave modes via mathematical model-based estimates. This can help to eliminate various sources of error such as composite manufacturing-related variabilities, material inhomogenities, and surface measurement noise on the reconstructed wave field. The averaging of velocity time history by multiple measurements is also helpful to eliminate random noise. Let us first consider the displacement field for in-plane and transverse wave motion based on the classical plate theory which gives the displacement field as

$$u(x,y,z,t) = u_0(x,y,t) - z\frac{\partial w_0(x,y,t)}{\partial x} \tag{1}$$

$$v(x,y,z,t) = v_0(x,y,t) - z\frac{\partial w_0(x,y,t)}{\partial y} \tag{2}$$

$$w(x,y,z,t) = w_0(x,y,t) \tag{3}$$

where u, v, w are the components of displacement at a material point along the x, y, and z axes respectively. u_0, v_0 are the in-plane displacements in the reference plane and w_0 is the transverse displacement defined at a point in the reference plane. The constitutive model for orthotropic laminated composites can be expressed as [46],

$$\begin{Bmatrix}\sigma_{xx}\\ \sigma_{yy}\\ \tau_{xy}\end{Bmatrix} = \begin{bmatrix}\overline{Q}_{11} & \overline{Q}_{12} & \overline{Q}_{16}\\ \overline{Q}_{21} & \overline{Q}_{22} & \overline{Q}_{26}\\ \overline{Q}_{16} & \overline{Q}_{26} & \overline{Q}_{66}\end{bmatrix}\begin{Bmatrix}\varepsilon_{xx}\\ \varepsilon_{yy}\\ \gamma_{xy}\end{Bmatrix} \tag{4}$$

where $\{\sigma\}$ and $\{\varepsilon\}$ are the stresses and strains (plane-stress approximation in the x–y plane is made where the laminate is thin), and $\overline{Q}_{ij}$ indicates the elastic constants in the plate coordinated after rotation of the material reference frame. Applying Hamilton's principle, the governing equations are expressed as

$$\begin{aligned}\delta u_0 : {} & A_{11}\frac{\partial^2 u_0}{\partial x^2} + 2A_{16}\frac{\partial^2 u_0}{\partial x\partial y} + A_{66}\frac{\partial^2 u_0}{\partial y^2} + A_{16}\frac{\partial^2 v_0}{\partial x^2}\\ & + (A_{12}+A_{66})\frac{\partial^2 v_0}{\partial x\partial y} + A_{26}\frac{\partial^2 v_0}{\partial y^2} - B_{11}\frac{\partial^3 w_0}{\partial x^3} - 3B_{16}\frac{\partial^3 w_0}{\partial x^2\partial y}\\ & - (B_{12}+2B_{66})\frac{\partial^3 w_0}{\partial x\partial y^2} - B_{26}\frac{\partial^3 w_0}{\partial y^3} - I_0\ddot{u}_0 + I_1\frac{\partial\ddot{w}_0}{\partial x} = 0\end{aligned} \tag{5}$$

$$\begin{aligned}\delta v_0 : {} & A_{16}\frac{\partial^2 u_0}{\partial x^2} + (A_{21}+A_{66})\frac{\partial^2 u_0}{\partial x\partial y} + A_{26}\frac{\partial^2 u_0}{\partial y^2} + A_{66}\frac{\partial^2 v_0}{\partial x^2}\\ & + 2A_{26}\frac{\partial^2 v_0}{\partial x\partial y} + A_{22}\frac{\partial^2 v_0}{\partial y^2} - B_{16}\frac{\partial^3 w_0}{\partial x^3} - (B_{21}+2B_{66})\frac{\partial^3 w_0}{\partial x^2\partial y}\\ & - 3B_{26}\frac{\partial^3 w_0}{\partial x\partial y^2} - B_{22}\frac{\partial^3 w_0}{\partial y^3} - I_0\ddot{v}_0 + I_1\frac{\partial\ddot{w}_0}{\partial y} = 0\end{aligned} \tag{6}$$

$$\begin{aligned}\delta w_0 : {} & B_{11}\frac{\partial^3 u_0}{\partial x^3} + 3B_{16}\frac{\partial^3 u_0}{\partial x^2\partial y} + (B_{21}+2B_{66})\frac{\partial^3 u_0}{\partial x\partial y^2} + B_{26}\frac{\partial^3 u_0}{\partial y^3}\\ & + B_{16}\frac{\partial^3 v_0}{\partial x^3} + B_{12} + 2B_{66}\frac{\partial^3 v_0}{\partial x^2\partial y} + 3B_{26}\frac{\partial^3 v_0}{\partial x\partial y^2} + B_{22}\frac{\partial^3 v_0}{\partial y^3}\\ & - D_{11}\frac{\partial^4 w_0}{\partial x^4} - 4D_{16}\frac{\partial^4 w_0}{\partial x^3\partial y} - (2D_{12}+4D_{66})\frac{\partial^4 w_0}{\partial x^2\partial y^2} - 4D_{26}\frac{\partial^4 w_0}{\partial x\partial y^3}\\ & - D_{22}\frac{\partial^4 w_0}{\partial y^4} - I_1\frac{\partial\ddot{u}_0}{\partial x} + I_2\left(\frac{\partial^2\ddot{w}_0}{\partial x^2} + \frac{\partial^2\ddot{w}_0}{\partial y^2}\right) - I_1\frac{\partial\ddot{v}_0}{\partial y} - I_0\ddot{w}_0 = 0\end{aligned} \tag{7}$$

where the stiffness coefficients A_{ij}, B_{ij}, and D_{ij} are functions of individual ply properties, ply orientation etc. and are integrated over the thickness as

$$[A_{ij}, B_{ij}, D_{ij}] = \sum_i \int_{z_i}^{z_{i+1}} \overline{Q}_{ij}[1, z, z^2]dz \tag{8}$$

Similarly, the coefficients associated with the inertial terms are expressed as

$$[I_0, I_1, I_2] = \sum_i \int_{z_i}^{z_{i+1}} \rho[1, z, z^2]dz \tag{9}$$

where z_i and z_{i+1} are the Z-coordinates of the lower and upper surfaces of the ith layer. The frequency domain spectral form of the displacement field is written in terms of time harmonic components, and spatially periodic wave modes in frequency (ω)-wavenumber (k) space (22), that is,

$$u_0(x,y,t) = \sum_{n=1}^{N} \tilde{u}_j e^{-i(k_x x + k_y y)} e^{i\omega_n t}, \tag{10}$$

$$v_0(x,y,t) = \sum_{n=1}^{N} \tilde{v}_j e^{-i(k_x x + k_y y)} e^{i\omega_n t}, \tag{11}$$

$$w_0(x,y,t) = \sum_{n=1}^{N} \tilde{w}_{0_j} e^{-i(k_x x + k_y y)} e^{i\omega_n t}, \tag{12}$$

where $i = \sqrt{-1}$, ω_n is the frequency at the nth sampling point, j indicates the mode of the wave where the number of modes to be determined from the characteristic equation in k–ω, and k_x, k_y are the wavenumbers in the x and y directions, respectively. The characteristic equation can be expressed as

$$\overline{A}_{mn} k_x^{m-1} k_y^{n-1} = 0 \tag{13}$$

where

$$\overline{A}_{11}(i,j) = 0,\ i \neq j; \quad \overline{A}_{11}(i,j) = I_0 \omega_n^2,\ i = j \tag{14}$$

$$\overline{A}_{12}(i,j) = 0,\ i \neq 2,\ j \neq 3\ \&\ i \neq 3,\ j \neq 3; \quad \overline{A}_{12}(2,3) = -\overline{A}_{12}(3,2) = iI_2\omega_n^2 \tag{15}$$

$$\overline{A}_{21}(i,j) = 0,\ i \neq 1,\ j \neq 3\ \&\ i \neq 3,\ j \neq 1; \quad \overline{A}_{21}(1,3) = -\overline{A}_{21}(3,1) = iI_1\omega_n^2 \tag{16}$$

$$\overline{A}_{13}(i,j) = \overline{A}_{13}(j,i); \quad \overline{A}_{13}(1,1) = -A_{66};\ \overline{A}_{13}(2,2) = -A_{22};\ \overline{A}_{13}(3,3) = I_2\omega_n^2;\ \overline{A}_{13}(1,2) = -A_{26};\ \overline{A}_{13}(1,3) = \overline{A}_{13}(2,3) = 0 \tag{17}$$

$$\overline{A}_{22}(i,j) = \overline{A}_{22}(j,i); \quad \overline{A}_{22}(1,1) = -2A_{16};\ \overline{A}_{22}(2,2) = -2A_{26};\ \overline{A}_{22}(1,2) = -A_{12} - A_{66};\ \overline{A}_{22}(3,3) = \overline{A}_{22}(1,3) = \overline{A}_{22}(2,3) = 0 \tag{18}$$

$$\overline{A}_{31}(i,j) = \overline{A}_{31}(j,i); \quad \overline{A}_{31}(1,1) = -iA_{11};\ \overline{A}_{31}(2,2) = -iA_{66};\ \overline{A}_{31}(3,3) = I_2\omega_n^2;\ \overline{A}_{31}(1,2) = -iA_{16}\overline{A}_{31}(1,3) = \overline{A}_{31}(2,3) = 0 \tag{19}$$

$$\overline{A}_{14}(i,j) = -\in_{ijk} w_k; \quad w = [iB_{22}, -iB_{26}, 0];\ \in_{123} = \in_{231} = \in_{312} = 1;\ \in_{132} = \in_{213} = \in_{321} = -1;\ \in_{ijk} = 0 \text{ otherwise} \tag{20}$$

$$\overline{A}_{23}(i,j) = -\in_{ijk} w_k; \quad w = [i3B_{26}, -i(B_{12} + 2B_{66}), 0];\ \in_{123} = \in_{231} = \in_{312} = 1;\ \in_{132} = \in_{213} = \in_{321} = -1;\ \in_{ijk} = 0 \text{ otherwise} \tag{21}$$

$$\overline{A}_{32}(i,j) = -\in_{ijk} w_k; \quad w = [i(B_{12} + 2B_{66}), -i3B_{16}, 0];\ \in_{123} = \in_{231} = \in_{312} = 1;\ \in_{132} = \in_{213} = \in_{321} = -1;\ \in_{ijk} = 0 \text{ otherwise} \tag{22}$$

$$\overline{A}_{41}(i,j) = -\in_{ijk} w_k; \quad w = [iB_{16}, -iB_{11}, 0] \tag{23}$$

$$\overline{A}_{15}(i,j) = 0,\ i \neq 3,\ j \neq 3; \quad \overline{A}_{15}(3,3) = -D_{22} \tag{24}$$

$$\overline{A}_{24}(i,j) = 0,\ i \neq 3,\ j \neq 3; \quad \overline{A}_{24}(3,3) = -4D_{26} \tag{25}$$

$$\overline{A}_{33}(i,j) = 0,\ i \neq 3,\ j \neq 3; \quad \overline{A}_{33}(3,3) = -2D_{12} - 4D_{66} \tag{26}$$

$$\overline{A}_{42}(i,j) = 0,\ i \neq 3,\ j \neq 3; \quad \overline{A}_{42}(3,3) = -4D_{16} \tag{27}$$

$$\overline{A}_{51}(i,j) = 0,\ i \neq 3,\ j \neq 3; \quad \overline{A}_{51}(3,3) = -D_{11} \tag{28}$$

The analytical dispersion curve for the quasi-isotropic laminate $(0/90/45/-45)_s$ used in the present work is shown in Fig. 5(a). Experimentally measured velocities are compared and they show good agreement. A five-cycle tone burst voltage signal is applied to the piezoceramic actuator. The excitation signal characteristics are shown in Fig. 5(b). The piezoceramic actuator converts voltage signals into mechanical strain. This mechanical strain generates elastic waves, which propagate throughout the thickness of the elastic medium and are guided by boundaries over a long distance with little amplitude loss. The procedure to compute effective near field displacement in the neighborhood of the piezoceramic actuator has been described in Ref. [47]. The near field structural response at 100 kHz near the location of the piezoceramic actuator has been captured using 3D scanning LDV (see Fig. 4(b)). The wave propagates beyond the near field with the velocity in each direction dictated by the resultant wavenumber k, which is given by $k = k_x\hat{i} + k_y\hat{j}$. $\hat{i}$ and $\hat{j}$ are the unit vectors in the x and y directions, respectively.

5. Results and discussions

5.1. Diagnosis with a remotely located single actuator

The piezoceramic actuator is located remotely at one end of the T-joint (see Fig. 3). The wave field generated remotely by the actuator scatters due to various structural features like free edge(s), web–flange interface, and delamination. The response signal at various grid points on the accessible face of the flange is acquired using 3D LDV with the test setting mentioned in Section 4. The wave field is visualized by interpolating a surface velocity response measured from all the grid points for a particular time stamp. The snapshots of guided wave fields at successive times are shown in Fig. 6. The ultrasonic contrast in the form of alternating bands (iso-contour lines) can be seen. The color bands indicate the velocity of the particle vibration on the surface of the flange. As discussed earlier, the piezoceramic actuator is excited in the frequency regime where the A0 mode in the flange is predominant.

The initiation of an elastic wave by the actuator on the flange is depicted in Fig. 6(a). Wave initiation is analogous to dropping a stone in a pond. The wave propagates in the form of ripples or wedges and the wave front shape is altered if the material is orthotropic. The direct incidence of an A0 mode wave packet with a web and joint filler on the back face of the flange has been shown in Fig. 6(b) and (c). The traction-free structural boundary reflects the entire wave packet. This reflected wave packet is superposed with later incident packets (see top and left edges of Fig. 6(c)). The overlap of the incident wave with the reflected wave expands progressively (see Fig. 6(a)–(d)). Any sudden distortion/discontinuity in the iso-contour wave field distribution of velocity in the propagating wave packet indicates a change in material properties (see Fig. 6(c) and (d)). Any change in the material stiffness can be attributed to a local geometric anomaly, or (and) a structural boundary/joint. The continuity of the fringe pattern is intact even when the propagating wave encounters structural features like a free edge and a web–flange interface. However, the region enclosed by the rectangle in Fig. 6(c) and (d) depicts a series of distortions and discontinuities in the iso-contour of the velocity field. A rectangular zone is clearly seen which indicates the actual location of delamination. Fig. 6(c) and (d) show the progression of the superposed incident and reflected wave packets from free edge(s), structural boundaries and delamination at successive time instants. The distortion and discontinuity of the iso-contour wave field is a first-hand source of information for confirming the presence of damage and other structural features. Furthermore, the damage severity could be quantified based on damage indices [48,49] or spectral power flow [50]. Details regarding this will be discussed later.

The presence of the embedded delamination in the laminate splits the base laminate into two sub-laminates. Each sub-laminate, both above and below the delamination, acts as a separate waveguide. The wavelength is modulated due to the sub-laminate

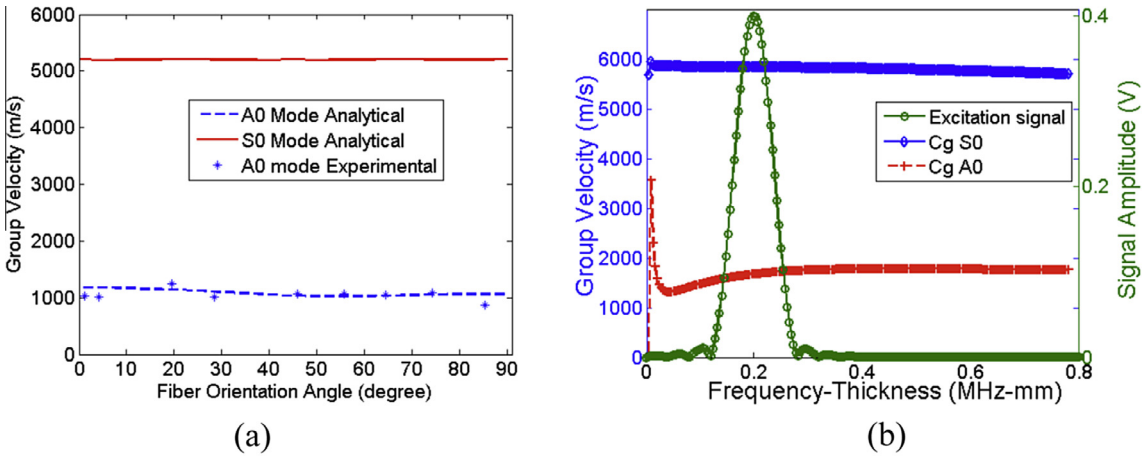

Fig. 5. (a) Dispersion curve for quasi-isotropic laminate $(0/90/45/-45)_s$. (b) Group velocity dispersion and signal characteristics used for ultrasonic wave excitation.

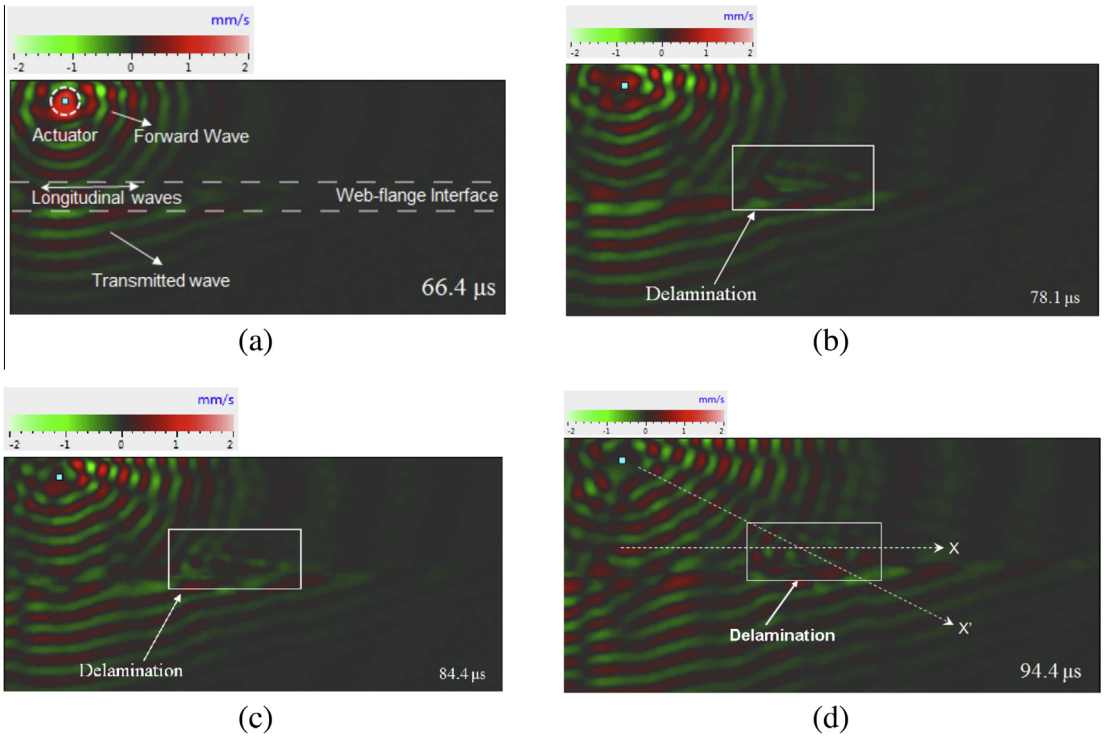

Fig. 6. Snapshots of surface velocity distribution on the flange at different time stamps (a) 66.4 µsec (b) 78.1 µsec (c) 84.4 µsec (d) 94.4 µsec.

splitting by the delamination. The delamination depth is identified by estimating the local wavelength modulation [19]. The local wavelength is estimated along both the horizontal and inclined line X and X′ respectively, which cuts across the delamination (see Fig. 6 (d)). The local wavelength variation at different time stamps is plotted along both the horizontal and inclined lines X and X′, respectively (see Fig. 7). The finding from the graph indicates the lowest value of the local wavelength in the zone of the delamination. Change in the local wavelength signifies change in local stiffness. Tracking wavelength along any scan line enables to identify change in the local stiffness either due to the structural boundary feature or due to local flaw(s). Findings from the local wavelength estimation along the horizontal (X) and inclined lines (X′) indicates that the tip of the delamination is approximately at a distance of 50 mm from the actuator and corresponding length and width of the delamination are approximately 50 mm (see Fig. 7(a)) and 20 mm (see Fig. 7 (b)), respectively. The T-joint was excited with predominant A0 mode whose incident wavelength is approximately, 11 mm. From Fig. 7 it could be inferred that the local wavelength in the region of the delamination is approximately half the incident wavelength. The ratio of local wavelength to incident wavelength correlates approximately to the ratio of square root of thickness of sub-laminate to square root of thickness of the base laminate. The surface of sub-laminate on which measurements are done is involved in this correlation. The depth of the delamination is about 0.8 mm from the accessible side of the flange. The increasing wavelength on one-side of the delamination can be attributed due to the mode conversion effect (from A0→ S0 mode).

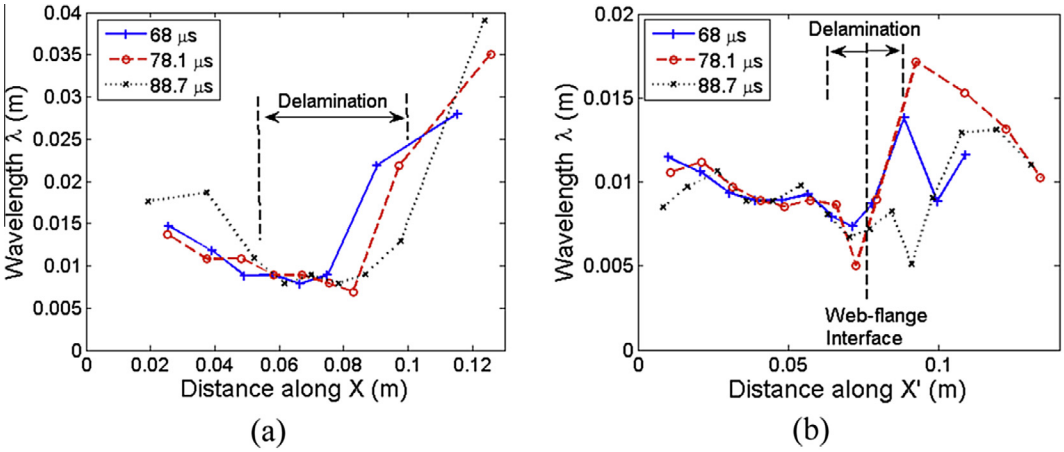

Fig. 7. Wavelength variation over time at different time snaps along (a) horizontal line X and (b) along inclined line X′ as marked in Fig. 5(d).

To analyze the non-stationary wave field, we compute the Root Mean Square (RMS) of the velocity–time field distribution. On considering a simple laminated plate segment, the incident A0 displacement field is given as

$$W(x,t) = \tilde{w}e^{-ik_x x}e^{i\omega t} \tag{29}$$

where $K_x \approx \sqrt{\omega}\sqrt[4]{\frac{\rho h}{D_{11}}}$ assuming a thin plate and $k_y \to 0$ for a straight wave front propagating in x .The tone burst excitation signal is expressed as

$$W(x,t) = \tilde{w}e^{-ik_x x}(1-\cos\omega_m t)\sin\omega_c t \tag{30}$$

where ω_m is the modulation frequency, ω_c is the central frequency (signal carrier frequency). The RMS of the displacement field is expressed as

$$W_{rms}(x) = \sqrt{\frac{1}{t_2-t_1}\int_{t_1}^{t_2} W(x,t)\overline{W}(x,t)dt} \tag{31}$$

where $\overline{W}(x,t)$ is the complex conjugate of $W(x,t)$, t_1 and t_2 are the cutoff bounds of the time window. Let $t_1 = 0$ and $t_2 = T_m$, where $T_m = \frac{2\pi}{\omega_m}$.

Further simplification gives

$$W_{rms}(x) = \frac{\sqrt{3}}{2}|\tilde{w}| \tag{32}$$

where $\tilde{w}$ is the incident wave amplitude (Eq. (29)). It is clear that the RMS of the wave field over the scan area is invariant with respect to space and time and only to a certain extent depends on the cylindrical loss of the wave-energy. However, if a new wave mode appears for some reason, it would create cross-correlated or uncorrelated effects, which will disturb the above invariance properties of the RMS of the field. We now show an RMS image of the wave propagation pattern in Fig. 8. The near field of the actuator can be clearly seen. The stationary effect of the web–flange interface and the delamination area are also clearly identifiable. The background, which is almost uniform, has the average intensity as expressed in [32]. The fading away of the image from the actuator can be attributed to cylindrical spreading loss and material damping. The color intensity in the RMS image gives an idea about the scattering strength from the structural feature/defect, and can be informative about identifying possible areas for further detailed detection study.

The measurement accuracy of the proposed technique is crucial for considering further investigation of its suitability in detection of delamination in composites. Various uncertainties such as measurement noise including effects of ambient lighting, temperature, sample orientation etc., can influence measurement accuracy. We repeated the measurements by introducing uncertainties in terms of random noise in the excitation signal applied to the piezo transducer and in terms of detection threshold defined with respect to measurement noise. Statistical data to determine the sensitivity and probability of damage detection (POD) has been demonstrated for plate with varying one-sided line crack using optical and ultrasonic based inspection techniques [51]. The POD curve helps to identify the sensitivity of the technique to determine a specific type of damage with a certain confidence level. In the present experiment different batches of co-cured co-bonded composite T-joint with varying damage sizes are created. The size of delamination in the web–flange interface vary from 5 mm to 20 mm. Scatter plot showing measured damage size using the proposed technique for different test samples is shown in Fig. 9. In the present experiment the% standard deviation for detecting damage parameters for 5 mm, 10 mm, 15 mm, and 20 mm damages are 17.8%, 10.4%, 8.6% and 8.2%, respectively.

5.2. Ultrasonic contrast enhancement by standing waves

The ultrasonic contrast image surrounding the web–flange interface and the delamination is enhanced using the concept of standing waves. The standing wave eliminates the need of additional wave filtering techniques like frequency–wavenumber filtering to be applied to the scan data. In the present experiment, two remotely located actuators on the inner side of the flange are used, which are equidistant from the web–flange interface (see Fig. 10). Both the actuators are excited with a 5 cycle tone burst signal (as detailed earlier) simultaneously. The flexural waves from both the actuators propagate and scatter at the web–flange interface leading to destructive interferential standing waves (see Fig. 11(a)–(e)). A stronger X-component along the web–flange interface propagates after these interference peaks and the corresponding velocities are faster because of the in-plane nature of this wave mode in the web underneath the flange.

The experiments have been conducted with similar test settings as mentioned in Section 4. The full wave field excited by the two actuators is visualized in the same manner as done earlier (see Fig. 11). At the web interface of the flange, flexural waves from the two actuators produce standing waves, which result in a longitudinal wave component traveling through the deltoid [52,53] (see Fig. 11(a) and (b)). The separated longitudinal waves are further scattered with the transmitted wave into the delamination

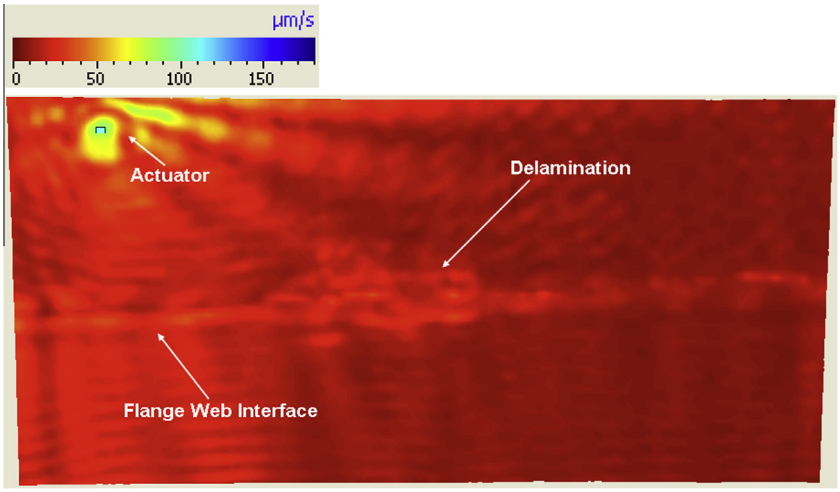

Fig. 8. Root Mean Square (RMS) velocity distribution for wave propagation and scattering with excitation frequency of 100 kHz.

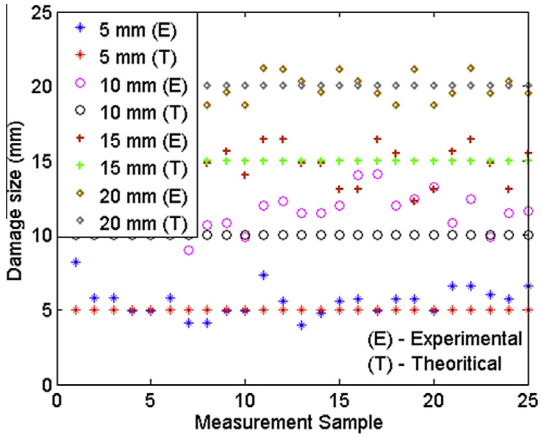

Fig. 9. Scatter plot showing measured damage size using the proposed technique for different test samples.

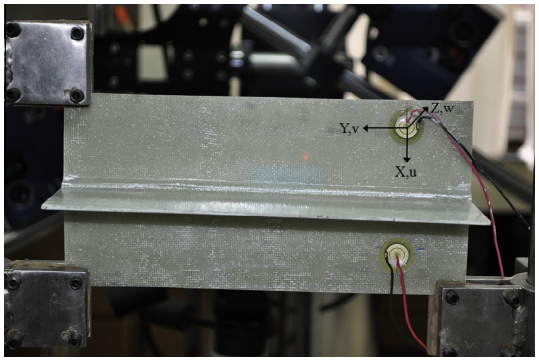

Fig. 10. Enlarged view of T-joint specimen with multiple actuators bonded on the back face of the flange to generate standing waves.

beneath the flange (see Fig. 11(c)–(e)). The insight gained from this experiment would help in developing a procedure to detect porous regions, fiber breakage in the deltoid at the junction of the web and flange, and the separability of waves in the presence of these other defects and delamination together.

5.3. Wave mode conversion due to boundary features and delamination

One of the important topics in guided wave analysis is the effect of material/structural features on wave mode conversion. The interaction of symmetric and anti-symmetric wave modes with geometric features has been addressed in the literatures [54–57] and the references therein. Depending on the geometrical perturbations, the reflections of waves from an anomaly or structural features, and the corresponding changes in the shape of the wave packet have been analyzed in Ref. [55]. The interaction of symmetric and anti-symmetric obstacles with guided waves has been studied in Refs. [24,56,58–60]. For a rapid inspection of the structural components, it is advantageous to analyze signals from a few selected scan points instead of scanning and analyzing the entire area. One such methodology using mode conversion strength is developed and discussed next which reduces the time and cost required to scan the entire structure for structural feature identification. The advantages of this method are that it is a baseline-free method, and, hence, does not require measurements of the original healthy structure. The identification of a structural feature or a defect using an array of virtual measurement points is possible. The method is suitable for monitoring the entire 360° around an actuator. The monitoring of a large area using fewer measurement points is also possible. The sparse scan points used in the analysis of wave mode conversion strength are selected based on the following criteria.

(1) The scan points are selected at far field locations at a distance greater than or equal to 2λ with respect to source location, where λ is the wavelength of the propagating wave corresponding to its carrier frequency.
(2) The scan points are spread equidistant from the actuator along a circular arc (see Fig. 14(a)). This ensures that the entire structure is covered using a compact arrangement of virtual circular array.

At each selected scan point in the virtual circular array, the following steps are executed to determine the wave mode conversion strength due to a delamination or other structural features.

Step 1 Measure velocity time histories at each scan point using scanning LDV. The measured signal includes both the incident wave packet(s) from the actuator and the reflected packet(s) from the various feature(s) (see Fig. 12(b)).

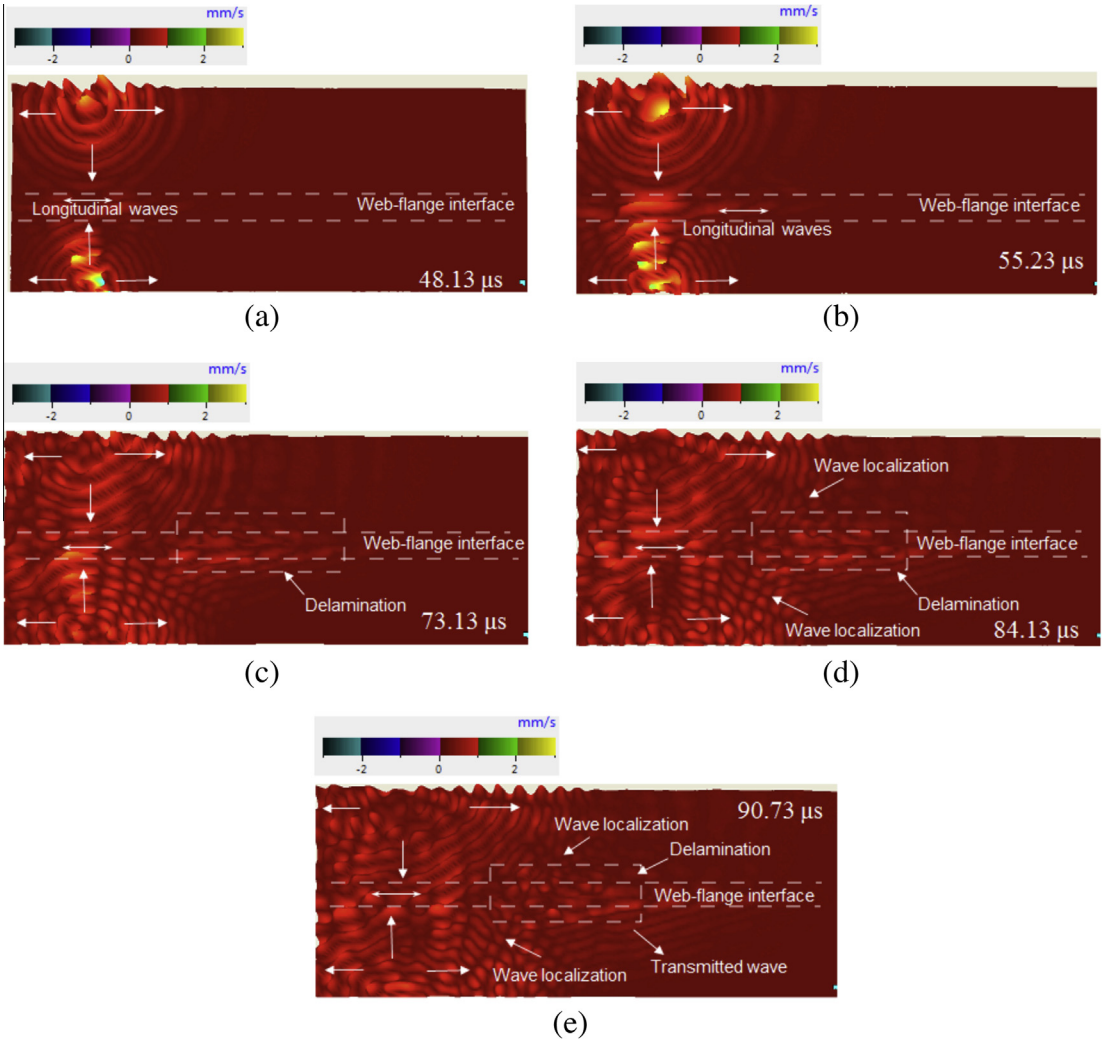

Fig. 11. Wave field visualization of velocity distribution for standing wave experiment at different time snaps of (a) 48.13 µsec (b) 55.23 µsec (c) 73.13 µsec (d) 84.13 µsec (e) 90.73 µsec.

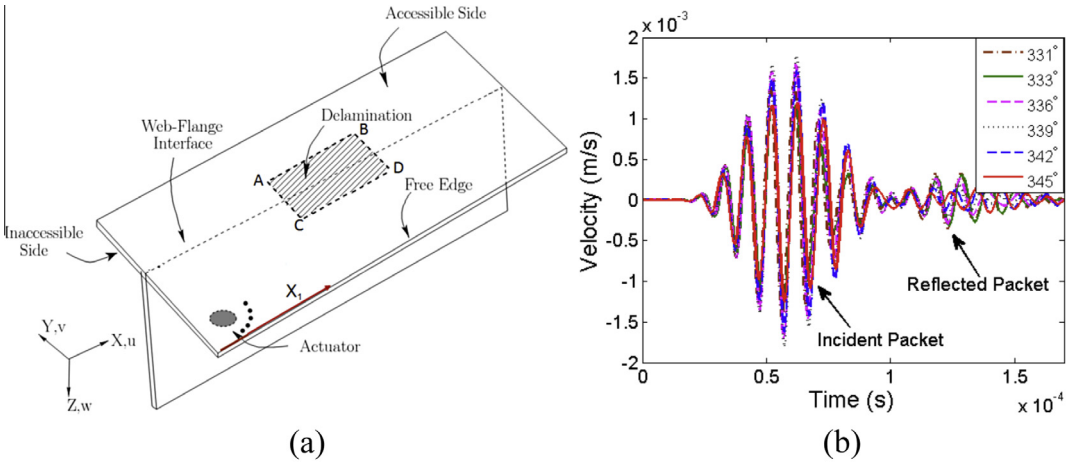

Fig. 12. (a) Schematic diagram showing T-joint with various structural features and sparse grid points corresponding to free-edge (X_1). (b) The first incident packet and the corresponding reflected packet for the out of plane component from the sparse grid points, which are at distance of 2λ with respect to actuator.

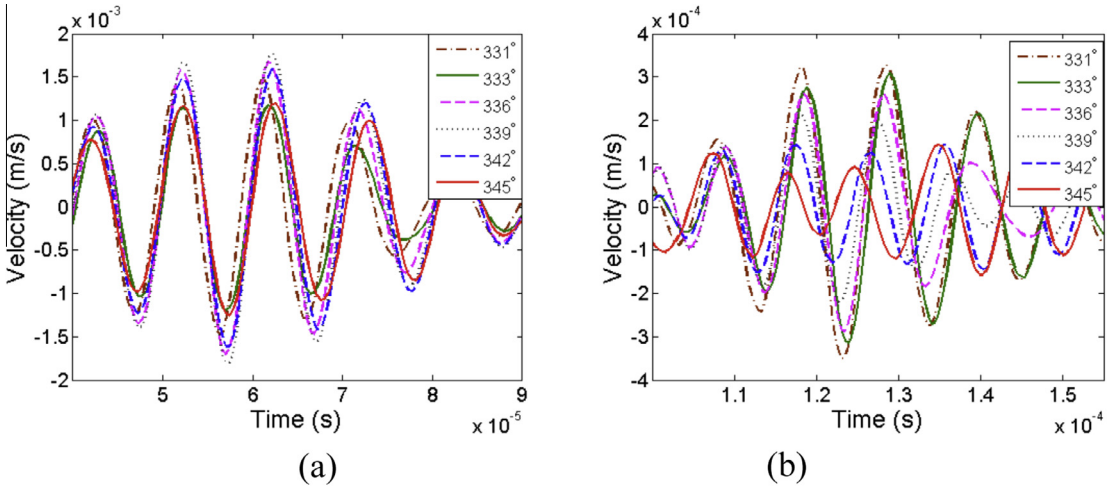

Fig. 13. (a) The extracted incident and (b) the reflected wave packet from sparse grid points corresponding to free-edge (X_1) (as marked in Fig. 12(a)).

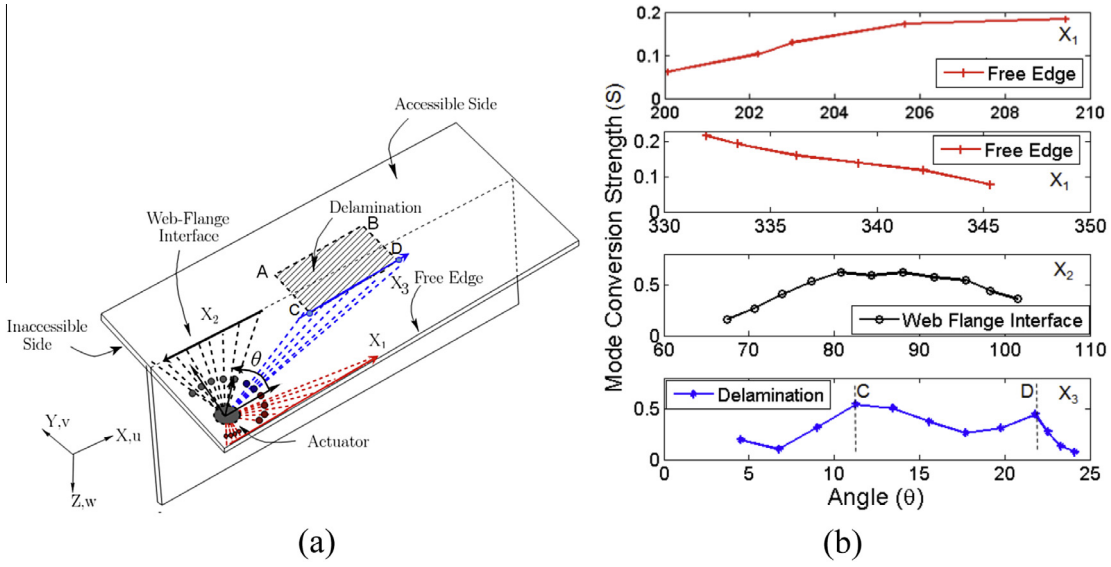

Fig. 14. (a) Schematic diagram showing T-joint with various structural features, scan regions used for wave mode conversion strength calculation. (b) Comparison of wave mode conversion strength among free-edge (X_1), web–flange interface (X_2) and delamination (X_3) as marked in (a).

Step 2 The incident wave packets and the reflected wave packets (see Fig. 13) are separated out from the original time signal using a moving window function. The width of the moving window function is given by the width of the excitation chirp signal.

Step 3 The center of the moving window in the time domain (T_{mov_window}) at each scan point is decided based on (a) group velocity (C_g) in that particular radial direction, and (b) the Euclidean distance between the actuator and the virtual sensing point (L_p). The center of the moving window at each scan point is given by

$$T_{mov\_window} = \frac{L_p}{C_g} \tag{33}$$

Step 4 The measured time signal in the moving window is converted to a frequency domain signal for both the incident packet and the reflected packet.

Step 5 The signal strength of the incident packet and the reflected packet are computed by summing up the amplitude in the frequency domain over the selected bandwidth. The bandwidth corresponds to the frequency range of the modulating signal that is used for generating the tone burst excitation signal.

Step 6 The wave mode conversion strength is estimated as

$$S_{M_i \to M_r} = \left| \frac{\hat{W}(x,\omega)_r}{\hat{W}(x,\omega)_i} \right| \tag{34}$$

where $\hat{W}(x,\omega)_r$ is the signal energy in the frequency domain corresponding to the reflected wave packet, $\hat{W}(x,\omega)_i$ is that of the incident wave packet, M_i and M_j are the incident and reflected wave modes, respectively.

Step 7 The mode conversion strength(s) is obtained at various scan points, which are at various polar angles of the radial line drawn outward from the actuator. (The angle θ is measured in counter clockwise direction with reference to the Cartesian coordinate system).

In the case of a free edge, it is observed that the mode conversion strength (S_{A0-S0}) decreases as the angles of oblique incidence increase (see Fig. 14(b)). The direct incidence, having a maximum energy of incidence at the free edge, occurs at 270°. As the angle of oblique incidence increases, the path length from the actuator to the free edge also increases accounting for increasing loss (cylindrical spreading and material attenuation). This, in turn, decreases the amplitude of the reflected wave packet measured at the scan point. The reflected signal energy is maximum when the path length is lowest and the incidence is normal to the structural boundary. In the case of the web–flange interface, the mode conversion strength distribution is a bell-shaped curve (see Fig. 14 (b)) while moving along the radial arc from 70° to 105°. The peak of the bell shaped curve occurs around 90° (normal incidence). The two results above show that the mode conversion strength increases to the maximum near normal incidence and decreases as the obliqueness of the incidence increases. Any additional local peak in the mode conversion strength apart from the peaks due to structural features like a free edge and a structural joint, indicates the possible presence of defects. This is verified when there is a delamination in the web–flange interface. In the case of a delamination in the web–flange interface, there are multiple peaks while moving in angular positions from 5° to 25°. This indicates the presence of certain anomalies. The multiple peaks are due to the delamination boundaries C and D (see Fig. 14(b)). Using this method, it is possible to investigate the entire structure and differentiate the structural features from the defects. Certain shadow regions between the delamination boundary D and the web flange interface are the limitations of this method. However, even with that, the method seems to be quite feasible for the inspection of integrally joined structure and where few scan points are sufficient instead of scanning the entire area.

6. Conclusions

This paper addresses the problems of (a) diagnosis of a complex composite structural joint like a co-cured co-bonded T-joint using a non-contact scanning laser Doppler velocimeter (b) detection of a delamination beneath the flange and along the web–flange interface using remotely-located actuator(s) (c) ultrasonic contrast enhancement using the concept of standing waves (d) mode conversion strength based identification and classification of features. The proposed technique is a baseline free technique. In this technique, a structural response is obtained only at a sparse number of grid points compared to full field data acquisition. The sparse grid points are in the form of a circular array, which is compact, and the area of monitoring is large. Important observations regarding non-contact guided wave ultrasonics in the composite are brought out. The insight gained from this experiment would be useful in developing a procedure to detect porous regions, fiber breakage in the deltoid at the junction of the web and flange, and to further study the separability of waves in the presence of these defects and delamination together.

Acknowledgements

The authors gratefully acknowledge financial support under the NPMASS Program, Government of India through Grant No. NPMA-12 to carry out this research.

References

[1] Boller C. Ways and options for aircraft structural health management. Smart Mater Struct 2001;10(3):432.
[2] Brand C, Boller C. Identification of life cycle cost reductions in structures with self-diagnostic devices. DTIC Document; 2000.
[3] LaRiviere SG, Thompson J, editors. Development of reliable NDI procedures for airframe inspection. NATO RTO meeting proc 10: airframe inspection reliability under field/depot conditions.
[4] Komorowski J, Simpson D, Gould R. A technique for rapid impact damage detection with implication for composite aircraft structures. Composites 1990;21(2):169–73.
[5] Lovejoy D. Magnetic particle inspection: a practical guide. Springer; 1993. David Lovejoy.
[6] De Goeje M, Wapenaar K. Non-destructive inspection of carbon fibre-reinforced plastics using eddy current methods. Composites 1992;23 (3):147–57.
[7] Wang X, Wong BS, Tui CG, Khoo KP, Foo F. Real-time radiographic non-destructive inspection for aircraft maintenance. In: 17th world conference on nondestructive testing, Shanghai, China. Citeseer.
[8] Szilard J. Ultrasonic testing: Non-conventional testing techniques. 605 Third Ave, New York, NY 10158: John Wiley & Sons, Inc; 1982. 640.
[9] Diamanti K, Soutis C. Structural health monitoring techniques for aircraft composite structures. Prog Aerosp Sci 2010;46(8):342–52.
[10] Baker W, McKenzie I, Jones R. Development of life extension strategies for Australian military aircraft, using structural health monitoring of composite repairs and joints. Compos Struct 2004;66(1):133–43.
[11] Speckmann H, Daniel JP, editors. Structural health monitoring for airliner, from research to user requirements, a European view. Conference on micro-nano-technologies.
[12] Assler H, Telgkamp J. Design of aircraft structures under special consideration of NDT. In: 9th ECNDT. p. 25–9.
[13] Doebling SW, Farrar CR, Prime MB. A summary review of vibration-based damage identification methods. Shock and vibration digest 1998;30 (2):91–105.
[14] Giurgiutiu V, Yu L, Kendall JR, Jenkins C. In-situ imaging of crack growth with piezoelectric-wafer active sensors. AIAA J 2007;45(11):2758–69.
[15] Rathod V, Mahapatra DR, editors. Estimation of fatigue damage parameters using guided wave technique. SPIE smart structures and materials+ nondestructive evaluation and health monitoring. International Society for Optics and Photonics; 2014.
[16] Rathod V, Roy Mahapatra D. Ultrasonic Lamb wave based monitoring of corrosion type of damage in plate using a circular array of piezoelectric transducers. NDT E Int 2011;44(7):628–36.
[17] Mustapha S, Ye L, Wang D, Lu Y. Assessment of debonding in sandwich CF/EP composite beams using A_0 Lamb wave at low frequency. Compos Struct 2011;93(2):483–91.
[18] Tan K, Guo N, Wong B, Tui C. Experimental evaluation of delaminations in composite plates by the use of Lamb waves. Compos Sci Technol 1995;53 (1):77–84.
[19] Nag A, Roy Mahapatra D, Gopalakrishnan S, Sankar T. A spectral finite element with embedded delamination for modeling of wave scattering in composite beams. Compos Sci Technol 2003;63(15):2187–200.
[20] Chakraborty A, Roy Mahapatra D, Gopalakrishnan S. Finite element analysis of free vibration and wave propagation in asymmetric composite beams with structural discontinuities. Compos Struct 2002;55(1):23–36.
[21] Wandowski T, Malinowski P, Kudela P, Ostachowicz W. Guided wave-based detection of delamination and matrix cracking in composite laminates. Proc Inst Mech Eng Part C: J Mech Eng Sci 2011;225(1):123–31.
[22] Gopalakrishnan S, Chakraborty A, Mahapatra DR. Spectral finite element method: wave propagation, diagnostics and control in anisotropic and inhomogeneous structures. Springer; 2007.
[23] Sreekanth Kumar D, Roy Mahapatra D, Gopalakrishnan S. A spectral finite element for wave propagation and structural diagnostic analysis of composite beam with transverse crack. Finite Elem Anal Des 2004;40(13):1729–51.
[24] Roy Mahapatra D, Gopalakrishnan S. A spectral finite element model for analysis of axial–flexural–shear coupled wave propagation in laminated composite beams. Compos Struct 2003;59(1):67–88.
[25] Kessler SS. Piezoelectric-based in-situ damage detection of composite materials for structural health monitoring systems. Massachusetts Institute of Technology; 2002.
[26] Kessler SS, Spearing SM, Soutis C. Damage detection in composite materials using Lamb wave methods. Smart Mater Struct 2002;11(2):269.
[27] Sastry C, Mahapatra DR, Gopalakrishnan S, Ramamurthy T. Distributed sensing of static and dynamic fracture in self-sensing piezoelectric composite: finite element simulation. J Intell Mater Syst Struct 2004;15(5):339–54.
[28] Sastry C, Mahapatra DR, Gopalakrishnan S, Ramamurthy T. Effect of the actuation phase on the SIF in delaminated composites with embedded piezoelectric layers. Smart Mater Struct 2003;12(4):602.
[29] Santos M, Santos J, Amaro A, Neto M. Low velocity impact damage evaluation in fiber glass composite plates using PZT sensors. Compos B Eng 2013;55:269–76.
[30] Su Z, Ye L, Bu X. A damage identification technique for CF/EP composite laminates using distributed piezoelectric transducers. Compos Struct 2002;57 (1):465–71.

[31] Ambroziński Ł, Stepinski T, Uh T. Efficient tool for designing 2D phased arrays in lamb waves imaging of isotropic structures. J Intell Mater Syst Struct 2014. 1045389X14545389.
[32] Lee SJ, Gandhi N, Hall JS, Michaels JE, Xu B, Michaels TE, et al. Baseline-free guided wave imaging via adaptive source removal. Struct Health Monit 2012;11(4):472–81.
[33] Wang L, Yuan F. Group velocity and characteristic wave curves of Lamb waves in composites: modeling and experiments. Compos Sci Technol 2007;67 (7):1370–84.
[34] Yan F, Rose JL, editors. Guided wave phased array beam steering in composite plates. The 14th international symposium on: smart structures and materials & nondestructive evaluation and health monitoring. International Society for Optics and Photonics; 2007.
[35] Rathod VT, Chakraborty N, Mahapatra DR, editors. Linear phased array of piezoelectric transducers for delamination monitoring in a composite laminate using Lamb waves. SPIE smart structures and materials+ nondestructive evaluation and health monitoring. International Society for Optics and Photonics; 2011.
[36] Sriram P. Whole field optical methods for structural mechanics: digital speckle correlation and laser Doppler velocimetry, 1988.
[37] Staszewski W, Lee B, Mallet L, Scarpa F. Structural health monitoring using scanning laser vibrometry: I. Lamb wave sensing. Smart Mater Struct 2004;13 (2):251.
[38] Mallet L, Lee B, Staszewski W, Scarpa F. Structural health monitoring using scanning laser vibrometry: II. Lamb waves for damage detection. Smart Mater Struct 2004;13(2):261.
[39] Leong W, Staszewski W, Lee B, Scarpa F. Structural health monitoring using scanning laser vibrometry: III. Lamb waves for fatigue crack detection. Smart Mater Struct 2005;14(6):1387.
[40] Staszewski W, Lee B, Traynor R. Fatigue crack detection in metallic structures with Lamb waves and 3D laser vibrometry. Meas Sci Technol 2007;18(3):727.
[41] An Y-K, Park B, Sohn H. Complete noncontact laser ultrasonic imaging for automated crack visualization in a plate. Smart Mater Struct 2013;22 (2):025022.
[42] Sohn H, Dutta D, Yang J, Park H, DeSimio M, Olson S, et al. Delamination detection in composites through guided wave field image processing. Compos Sci Technol 2011;71(9):1250–6.
[43] Park B, Sohn H, Yeum C-M, Truong TC. Laser ultrasonic imaging and damage detection for a rotating structure. Struct Health Monit 2013;12(5–6):494–506.
[44] Ruzzene M. Frequency–wavenumber domain filtering for improved damage visualization. Smart Mater Struct 2007;16(6):2116.
[45] Sharma VK. Laser doppler vibrometer for efficient structural health monitoring. ProQuest; 2009.
[46] Reddy JN. Mechanics of laminated composite plates and shells: theory and analysis. CRC Press; 2004.
[47] Rathod VT, Mahapatra DR, editors. Ultrasonic-guided wave-sensing properties of PVDF thin film with inter digital electrodes. SPIE smart structures and materials+ nondestructive evaluation and health monitoring. International Society for Optics and Photonics; 2014.
[48] Geetha GK, Rathod V, Chakraborthy N, Mahapatra DR, Gopalakrishnan S. Rapid localization and ultrasonic imaging of multiple damages in structural panel with piezoelectric sensor-actuator network. In: Proc IWSHM. p. 249–56.
[49] Giridhara G, Rathod V, Naik S, Roy Mahapatra D, Gopalakrishnan S. Rapid localization of damage using a circular sensor array and Lamb wave based triangulation. Mech Syst Signal Process 2010;24(8):2929–46.
[50] Mahapatra DR, Gopalakrishnan S. Spectral finite element analysis of coupled wave propagation in composite beams with multiple delaminations and strip inclusions. Int J Solids Struct 2004;41(5):1173–208.
[51] Geetha KG, Ravi NB, Chakraborty N, Ukirde KC, Kamalakar G, Mahapatra D. Damage detection sensitivity, specificity and classification data analysis for shm systems design, verification and validation; 2015.
[52] Chen J, Ravey E, Hallett S, Wisnom M, Grassi M. Prediction of delamination in braided composite T-piece specimens. Compos Sci Technol 2009;69 (14):2363–7.
[53] Trask R, Hallett S, Helenon F, Wisnom M. Influence of process induced defects on the failure of composite T-joint specimens. Compos A Appl Sci Manuf 2012;43(4):748–57.
[54] Alleyne DN, Cawley P. The interaction of Lamb waves with defects. IEEE Trans Ultrason Ferroelectr Freq Control 1992;39(3):381–97.
[55] Basri R, Chiu WK. Numerical analysis on the interaction of guided Lamb waves with a local elastic stiffness reduction in quasi-isotropic composite plate structures. Compos Struct 2004;66(1):87–99.
[56] Benmeddour F, Grondel S, Assaad J, Moulin E. Study of the fundamental Lamb modes interaction with asymmetrical discontinuities. NDT E Int 2008;41 (5):330–40.
[57] Xu K, Ta D, Su Z, Wang W. Transmission analysis of ultrasonic Lamb mode conversion in a plate with partial-thickness notch. Ultrasonics 2014;54 (1):395–401.
[58] Ahmad ZAB. Numerical simulations of Lamb waves in plates using a semi-analytical finite element method: Magdeburg, Universität, Diss., 2011; 2011.
[59] Cho Y. Estimation of ultrasonic guided wave mode conversion in a plate with thickness variation. IEEE Trans Ultrason Ferroelectr Freq Control 2000;47 (3):591–603.
[60] Mahapatra DR, Gopalakrishnan S, Sankar T. Spectral-element-based solutions for wave propagation analysis of multiply connected unsymmetric laminated composite beams. J Sound Vib 2000;237(5):819–36.